Frontiers of Information Technology & Electronic Engineering
www.jzus.zju.edu.cn; engineering.cae.cn; www.springerlink.com
ISSN 2095-9184 (print); ISSN 2095-9230 (online)
E-mail: jzus@zju.edu.cn

On robustness of an AMB suspended energy storage flywheel platform under characteristic model based all-coefficient adaptive control laws*

Xujun LYU‡[1], Long DI[2], Zongli LIN[3]

[1]*College of Engineering, Huazhong Agricultural University, Wuhan 430070, China*

[2]*ASML-HMI, CA 95131, USA*

[3]*Charles L. Brown Department of Electrical and Computer Engineering, University of Virginia, VT 22904-4743, USA*

E-mail: lyuxujun@mail.hzau.edu.cn; ld4vv@virginia.edu; zl5y@virginia.edu

Received Sept. 28, 2018; Revision accepted Dec. 25, 2018; Crosschecked Jan. 8, 2019

Abstract: A characteristic model based all-coefficient adaptive control law was recently implemented on an experimental test rig for high-speed energy storage flywheels suspended on magnetic bearings. Such a control law is an intelligent control law, as its design does not rely on a pre-established mathematical model of a plant but identifies its characteristic model while the plant is being controlled. Extensive numerical simulations and experimental results indicated that this intelligent control law outperforms a μ-synthesis control law, originally designed when the experimental platform was built in terms of their ability to suppress vibration on the high-speed test rig. We further establish, through an extensive simulation, that this intelligent control law possesses considerable robustness with respect to plant uncertainties, external disturbances, and time delay.

Key words: Intelligent control; Robustness; Uncertainty; Disturbance rejection; Active magnetic bearings; Energy storage flywheels

https://doi.org/10.1631/FITEE.1800606 **CLC number:** TP13

1 Introduction

Recent technological advances have drastically increased renewable energy generations, such as wind power generation, solar photovoltaic power generation, and hydraulic power generation. Then, the proportion of renewable energy contributing to the power grid is rapidly increasing, bringing about an urgent demand for the energy storage technology (Zhao et al., 2015). Indeed, energy storage technologies have been assumed to be a critical role in ensuring safe, stable, and economic operation of the power grid by solving the volatility and intermittent problems associated with the renewable energy that flows into the power grid (Koohi-Kamali et al., 2013). Among these technologies is the mechanical energy storage, represented by flywheel energy storage systems. With their advantages of short recharge time, high energy efficiency, high power density, tolerance to extreme temperature, and durability (Hebner et al., 2002; Mousavi G et al., 2017), energy storage flywheels have found many applications both as energy storage devices in power systems and in simultaneous energy storage and attitude control during space missions (Reid et al., 2013; Farhadi and Mohammed, 2016).

A flywheel suspended on active magnetic bearings (AMBs) is a complex system consisting of a rotor, AMBs with control systems, auxiliary bearings,

‡ Corresponding author

* Project supported by the Fundamental Research Funds for the Central Universities, China (No. 2662018QD031)

ORCID: Xujun LYU, http://orcid.org/0000-0002-2466-2338

flywheel disks, and energy conversion mechanisms. During the charging phase, the kinetic energy is stored in flywheel disks and is released to the load in the discharging phase (Zhao et al., 2015). Their appealing features of no friction, no lubrication, low losses, no wear, fast response, and long lifetime (Schweitzer and Maslen, 2009) make AMBs a ideal support of flywheel rotors for high-speed operation. However, AMBs rely on control systems for their operation. It has been well known that AMB control systems for high-performance energy storage flywheels are rather sophisticated (Li et al., 2006).

Because of its complexity, the construction of an AMB suspended flywheel test rig is often costly for a research laboratory. Recently, we developed, from an existing flexible rotor-AMB test rig in the ROtating MAchinery and Controls (ROMAC) laboratory at the University of Virginia, an experimental platform for AMB suspended energy storage flywheels (Lyu et al., 2016). This platform served as a high-speed flywheel AMB test rig to assist in analysis and design of high-speed flywheel AMB control systems. A high-fidelity simulation model was simultaneously developed.

Various control design methods, including the classical methods (such as proportional-integral-derivative (PID) control (Dever et al., 2004; Brown et al., 2005; Peng et al., 2017)) and modern control theory (such as H_∞ control (Sivrioglu et al., 2004) and μ-synthesis (Mushi et al., 2012)), have been explored for AMB control systems. PID control is simple but less effective in dealing with complex rotordynamics. Modern control design methods are more effective but usually require a model of plant and a characterization of uncertainties. Di and Lin (2014) explored the application of characteristic model based all-coefficient adaptive control (ACAC), originally proposed by Wu et al. (2007, 2009), to the ROMAC flexible rotor-AMB test rig mentioned above, and led to lower levels of vibration than that of a benchmark μ-synthesis controller. The ACAC law is an intelligent control law because its design does not rely on a pre-established mathematical model of the plant but identifies its characteristic model while the plant is being controlled.

Two different control designs have been implemented on the abovementioned experimental platform for AMB suspended energy storage flywheels: the μ-synthesis control originally designed when the experimental platform was built (Lyu et al., 2016) and the characteristic model based ACAC (Lyu et al., 2018a). Extensive numerical simulations and experimental results indicated that, despite its simplicity, the characteristic model based ACAC law outperforms the original μ-synthesis control law in terms of their ability to suppress vibration on the high-speed flywheel AMB test rig. Furthermore, numerous simulations and experimental results validated that the simulation model accurately predicts the experimental results (Lyu et al., 2016). Lyu et al. (2018b) observed that the characteristic model based ACAC law possesses considerable ability to resist the adverse effects of time delay in the measurement of control inputs and/or outputs.

We establish a characteristic model based ACAC law possessing considerable robustness with respect to plant uncertainties, external disturbances, and time delay through extensive simulations.

2 Characteristic model based ACAC design for the flywheel experimental platform

Lyu et al. (2018a) implemented the characteristic model based ACAC design on the experimental platform (Lyu et al., 2016) that we previously developed as a test rig for flywheel AMB system control designs. In this section, we briefly review some results in Lyu et al. (2018a).

2.1 AMB suspended flywheel test rig

Based on the finite element method, the rotordynamic model of the flywheel AMB system is derived from the motion equation described as

$$\boldsymbol{M}\ddot{\boldsymbol{q}}+(\boldsymbol{C}+\Omega\boldsymbol{G})\dot{\boldsymbol{q}}+\boldsymbol{K}\boldsymbol{q}=\boldsymbol{B}_{\mathrm{m}}\boldsymbol{F}_{\mathrm{mag}}+\boldsymbol{B}_{\mathrm{e}}\boldsymbol{F}_{\mathrm{ext}}, \quad (1)$$

where $\boldsymbol{M}$ is the symmetric flywheel rotor mass matrix, $\boldsymbol{C}$ the symmetric damping matrix, $\boldsymbol{G}$ the skew-symmetric gyroscopic effect matrix, $\boldsymbol{K}$ the symmetric stiffness matrix, Ω the rotational speed, $\boldsymbol{B}_{\mathrm{m}}$ the position distribution matrix of the support AMBs, $\boldsymbol{F}_{\mathrm{mag}}$ the forces provided by support AMBs, $\boldsymbol{B}_{\mathrm{e}}$ the position distribution matrix of the external forces, $\boldsymbol{F}_{\mathrm{ext}}$ the external forces acting on the rotor, and $\boldsymbol{q}$ the generalized displacement vector.

Compared with a usual rotor-AMB system, two important features of an AMB suspended flywheel system are the negative stiffness of a generator and

the gyroscopic effects caused by a flywheel disk (Hebner et al., 2002). Lyu et al. (2016) emulated operation of an energy storage flywheel on an existing flexible rotor-AMB test rig and developed an experimental platform to serve as a test rig for high-speed flywheel AMB control designs. The flexible AMB suspended rotor in the ROMAC (Mushi et al., 2012) is shown in Fig. 1. Specifically, we use two support AMBs at the driven end (DE) and non-driven end (NDE) of the rotor as control AMBs that stabilize the system operation. We use the exciter AMB (or the disturbance AMB) at the quarter span to emulate the negative stiffness of the generator and two exciter AMBs to generate gyroscopic coupling resulting from the flywheel disk (Fig. 2).

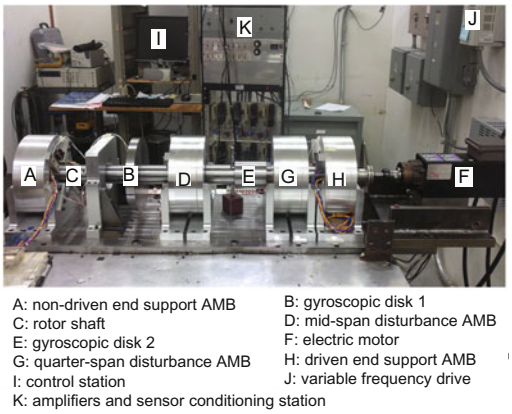

Fig. 1 A flexible rotor-AMB test rig

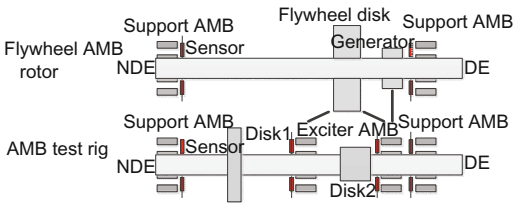

Fig. 2 Schematic of the experimental platform for AMB suspended flywheels

The main components of the ROMAC flexible rotor-AMB test rig are described as follows:

1. Rotor. The flexible rotor measures 1.23 m in length and 44.9 kg in mass. A 3.7-kW motor with a variable frequency drive (Colombo RS-90/2) is equipped to spin the rotor to speed up to 18 000 r/min. The drive is connected to a flexible disk coupling, Rexnord 75CC140140, through a custom shaft extension.

2. AMBs. A laminated steel journal is mounted on the rotor for each of the four radial AMBs. An auxiliary ball bearing is mounted at the location of each of the two support AMBs to protect them from damage in case of a rotor drop.

3. Digital controller. The digital controller is implemented on an innovative integration M6713 PCI board with a TI C6713B 32-bit floating-point DSP chip. Sixteen input-output analog channels, which link the 16 sensors to the 16 actuators of the four AMBs, are simultaneously sampled at a sampling frequency of 12 kHz.

4. Amplifier. Each AMB is driven by a Copley control PWM amplifier, which operates from a 150-V DC power supplying a continuous current rating of 10 A to provide a maximum static load of 1450 N.

5. Displacement sensors. A Kaman 1-H/15-N eddy current probe measures the rotor position at the location of each support AMB, and an anti-alias filter circuit attenuates the measurement noise. A Bently Nevada 7200 Series eddy current probe, whose output voltage is changed from −10 to 0 V by a gain and offset circuit, measures the rotor motion at the location of each exciter AMB.

2.2 Characteristic model based ACAC

A basic idea of characteristic modeling is that a higher-order system can be equivalently represented as a lower-order, often first- and second-order, time-varying linear system, which, when the sampling period is sufficiently small, has the same output as the original system at the sampling instants. This lower-order system is called the "characteristic model of the original system" (Wu et al., 2007, 2009). The time-varying coefficients of the characteristic model, referred to as the characteristic parameters, are then identified online adaptively. Based on the characteristic model, a simple PID control law is designed. The resulting feedback law is referred to as the characteristic model based ACAC law. A schematic of the characteristic model based ACAC system is shown in Fig. 3.

2.2.1 Characteristic modeling

Considering a linear time-invariant plant described as

$$G(s)=\frac{b_m s^m+b_{m-1}s^{m-1}+\ldots+b_1 s+b_0}{s^n+a_{n-1}s^{n-1}+\ldots+a_1 s+a_0}, \quad (2)$$

where a_i and b_j ($i=0,1,\ldots,n-1$ and $j=0,1,\ldots,m$) are constant parameters of the plant. If the control objective is position keeping or reference tracking, and the sampling period T is sufficiently small (Wu et al., 2007, 2009), the characteristic model takes

$$\begin{aligned} y(k) =& f_1(k)y(k-1)+f_2(k)y(k-2) \\ &+g_0(k)u(k-1)+g_1(k)u(k-2), \end{aligned} \quad (3)$$

where $u(k)$ is the control input, $y(k)$ the system output, and $f_1(k)$, $f_2(k)$, $g_0(k)$, and $g_1(k)$ the characteristic parameters which can be identified by a gradient adaptive law. It has been established that the characteristic model produces the same output as the original plant model (2) at each sampling instant providing that the sampling is fast enough.

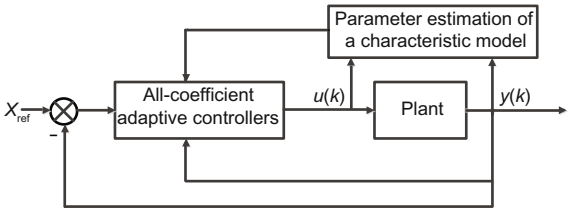

Fig. 3 Diagram of the characteristic model based ACAC system

2.2.2 Characteristic model based ACAC

The characteristic model based ACAC law takes

$$u_{\mathrm{c}}(k)=u_{\mathrm{O}}(k)+u_{\mathrm{G}}(k)+u_{\mathrm{D}}(k)+u_{\mathrm{I}}(k), \quad (4)$$

where $u_{\mathrm{O}}(k)$ is the maintaining/tracking control, $u_{\mathrm{G}}(k)$ the golden section adaptive control, $u_{\mathrm{D}}(k)$ the differential control, and $u_{\mathrm{I}}(k)$ the integral control, which are given by $u_{\mathrm{O}}(k)=\frac{y_{\mathrm{r}}(k)-\hat{f}_1(k)y(k)-\hat{f}_2(k)y(k-1)-\hat{g}_1(k)u_{\mathrm{O}}(k-1)}{\hat{g}_0(k)+\lambda_1}$, $u_{\mathrm{G}}(k)=\frac{l_1\hat{f}_1(k)\tilde{y}(k)+l_2\hat{f}_2(k)\tilde{y}(k-1)+\hat{g}_1(k)u_{\mathrm{G}}(k-1)}{\hat{g}_0(k)+\lambda_1}$, $u_{\mathrm{D}}(k)=d_1\frac{\tilde{y}(k)-\tilde{y}(k-1)}{T}$, and $u_{\mathrm{I}}(k)=d_1\frac{\tilde{y}(k)-\tilde{y}(k-1)}{T}$, where $y_{\mathrm{r}}(k)$ is the reference output, λ_1 is a positive constant, $\tilde{y}(k)=y_{\mathrm{r}}(k)-y(k)$, $l_1=0.382$, $l_2=0.618$, and d_1 and d_2 are positive constants.

2.3 Simulations and experimental results

Simulations of the rotor displacements without and with the generator negative stiffness show that the effect caused by a generator is minimal and negligible (Lyu et al., 2016). In the simulations of the rotor orbits with an actual gyroscopic matrix $\boldsymbol{G}$ and the emulated gyroscopic forces, the similar patterns and orbits tilting phenomena indicate the feasibility of the flywheel emulation approach. All the simulations are verified by the experimental results. Therefore, we provided an experimental flywheel AMB platform to study the control design for energy storage flywheels (Lyu et al., 2016).

Because of the complex dynamics and presence of strong uncertainties, the flywheel AMB system was first stabilized by the μ-synthesis controller. Then, the characteristic model based ACAC design was implemented on this flywheel emulation platform to study the flywheel control design. An identical characteristic model based ACAC law, as a substitute for the μ-synthesis controller, was implemented for each of the four control channels and the x and y axes of the two support AMBs. Fig. 4 shows the simulated rotor orbits under the μ-synthesis controller compared with the corresponding orbits under the characteristic model based ACAC, where the polar moment of inertia of the emulated flywheel was $J_{\mathrm{p}}=0.021\,\mathrm{kg\cdot m^2}$, the transverse moment of inertia was $J_{\mathrm{t}}=0.5J_{\mathrm{p}}$, and the rorational speed was $\Omega=7600\,\mathrm{r/min}$. In Fig. 4 and some other figures, the four plots, dn$x$-dn$y$, dm$x$-dm$y$, dq$x$-dq$y$, and dd$x$-dd$y$, are orbits at the locations of the non-driven end bearing, mid-span bearing, quarter-span bearing, and driven end bearing, respectively. It is observed that the displacements in both x and y axes at the locations of the two support AMBs are small under the characteristic model based ACAC.

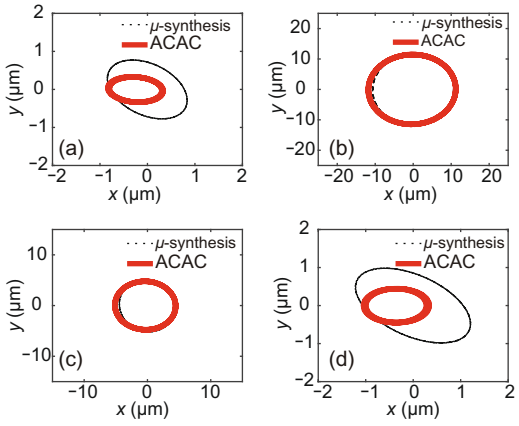

Fig. 4 Simulated rotor orbits at $\Omega=7600\,\mathrm{r/min}$ under the μ-synthesis controller and characteristic model based ACAC: (a) dn$x$-dn$y$; (b) dm$x$-dm$y$; (c) dq$x$-dq$y$; (d) dd$x$-dd$y$

Fig. 5 shows a comparison of the experimental rotor orbits under two controllers with $J_p = 0.021\,\mathrm{kg{\cdot}m^2}$ and $\Omega = 7600$ r/min. The thin curves are the experimental results under the μ-synthesis controller and the thick curves are the rotor orbits under the characteristic model based ACAC law. We can observe that the characteristic model based ACAC design results in smaller rotor orbits at all AMB locations than the μ-synthesis controller, which approximately represents a 50% reduction in the vibration at the location of the NDE AMB, a 60% reduction at the locations of the two exciter AMBs, and a 25% reduction at the location of the DE AMB. That is to say, the simulations and experimental results validate that the characteristic model based ACAC can achieve a better vibration suppression of the AMB suspended energy storage flywheel test rig than the μ-synthesis controller.

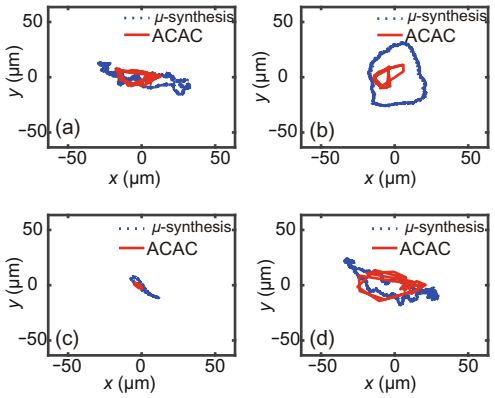

Fig. 5 Experimental rotor orbits at $\Omega = 7600$ r/min under the μ-synthesis controller and characteristic model based ACAC: (a) dn$x$-dn$y$; (b) dm$x$-dm$y$; (c) dq$x$-dq$y$; (d) dd$x$-dd$y$

3 Robustness with respect to plant uncertainties

Because the characteristic model based ACAC control law identifies the characteristic model of the plant when it is being controlled and its design does not rely on an existing model of the plant, it will continue to perform when the plant changes; that is to say, by its design mechanism, the characteristic model based ACAC law is robust to plant uncertainties. In this section, we provide some simulations to illustrate this robustness.

In the results we reviewed in Section 2, the emulated flywheel has a polar moment of inertia $J_p = 0.021\,\mathrm{kg{\cdot}m^2}$ and a transverse moment of inertia $J_t = 0.5J_p$ and operates at a rotational speed of $\Omega = 7600$ r/min. We apply the same characteristic model based ACAC law to differently emulated flywheels with polar moments of inertia $J_p = 0.042$, 0.084, and 0.105 $\mathrm{kg{\cdot}m^2}$, respectively. The orbits of these emulated flywheels are plotted in Figs. 6–8. For comparison, the orbits of the emulated flywheel with $J_p = 0.021\,\mathrm{kg{\cdot}m^2}$ are re-plotted in Fig. 9. Orbits remain similar in size as the plant parameters vary in a large range, which indicates strong robustness of the characteristic model based ACAC laws with respect to plant uncertainties.

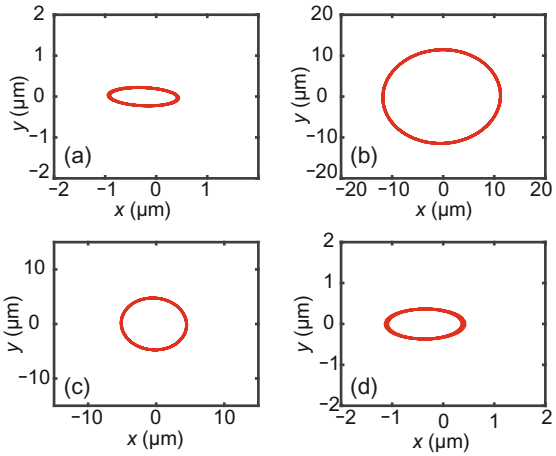

Fig. 6 Rotor orbits at $\Omega = 7600$ r/min of an emulated flywheel with $J_p = 0.042$ kg·m^2 under characteristic model based ACAC laws: (a) dn$x$-dn$y$; (b) dm$x$-dm$y$; (c) dq$x$-dq$y$; (d) dd$x$-dd$y$

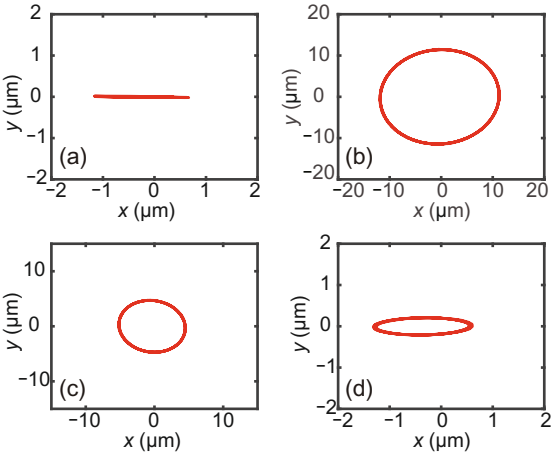

Fig. 7 Rotor orbits at $\Omega = 7600$ r/min of an emulated flywheel with $J_p = 0.084$ kg·m^2 under characteristic model based ACAC laws: (a) dn$x$-dn$y$; (b) dm$x$-dm$y$; (c) dq$x$-dq$y$; (d) dd$x$-dd$y$

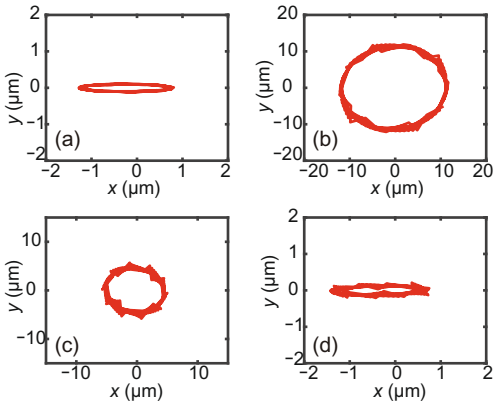

Fig. 8 Rotor orbits at $\Omega = 7600$ r/min of an emulated flywheel with $J_p = 0.105$ kg·m^2 under characteristic model based ACAC laws: (a) dn$x$-dn$y$; (b) dm$x$-dm$y$; (c) dq$x$-dq$y$; (d) dd$x$-dd$y$

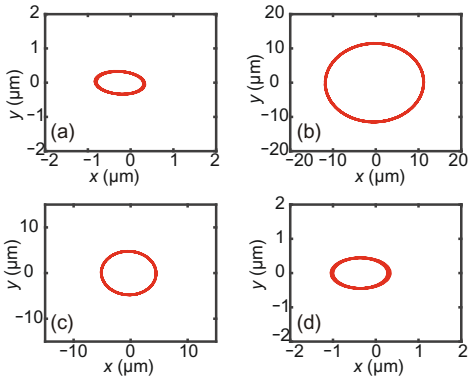

Fig. 9 Rotor orbits at $\Omega = 7600$ r/min of an emulated flywheel with $J_p = 0.021$ kg·m^2 under characteristic model based ACAC laws: (a) dn$x$-dn$y$; (b) dm$x$-dm$y$; (c) dq$x$-dq$y$; (d) dd$x$-dd$y$

4 Robustness with respect to external disturbances

In the operation of an AMB suspended energy storage flywheel, disturbances derived from external sources often affect the system performance and even cause instability. External disturbances arise from machine base motions caused by operating the flywheel in a moving vehicle or for a tidal power generation. External disturbances could arise from the external factors that cause the system to be off balance. Depending on their sources, disturbances could be constant or periodic function of time. In this section, we investigate the capacity of the characteristic model based ACAC laws in resisting these two forms of disturbances.

4.1 Constant disturbances

In this subsection, we consider constant disturbances that are presented in the inputs to all four AMBs. In our simulations, we apply the same characteristic model based ACAC laws to the flywheel AMB system with the polar moment of inertia $J_p = 0.021\,\text{kg·m}^2$ at the rotational speed of $\Omega = 7600$ r/min. In each of the three simulation runs, constant disturbances in the form of Δi are set to be 0.1, 0.3, and 0.5 A. These currents represent forces of 10–50 N for the four different bearings in our experimental platform.

Figs. 10–12 show the rotor displacements at four AMBs. Table 1 shows the peak rotor displacements at each AMB under these three constant disturbance values.

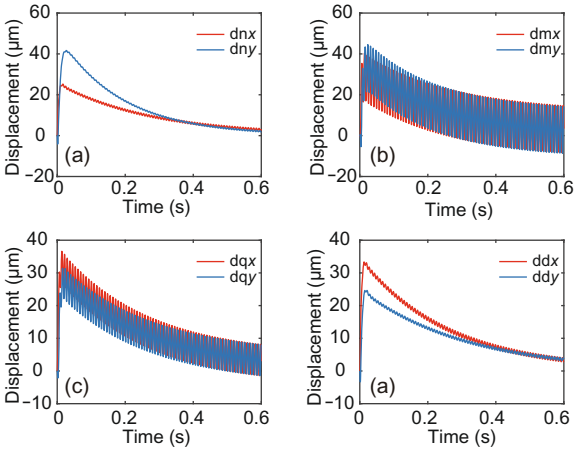

Fig. 10 Rotor displacements at $\Omega = 7600$ r/min of an emulated flywheel with $J_p = 0.021$ kg·m^2 and Δi=0.1 A, under characteristic model based ACAC laws: (a) NDE; (b) MID; (c) QTR; (d) DE

Rotor orbits are plotted in Figs. 13–15. As summarized in Table 1, the peak values of rotor displacements increase as the magnitude of the constant disturbance current increases. However, the maximum amplitudes of the rotor displacements at the four AMB locations at the x and y axes under the three different disturbance currents are 0.45×10^{-4}, 1.24×10^{-4}, and 2.07×10^{-4} m, respectively. All these maximum displacements are well within the air gaps of the AMBs, indicating that the characteristic model based ACAC laws resist the adverse effects of the disturbances very well and that the system robustly performs with constant disturbances.

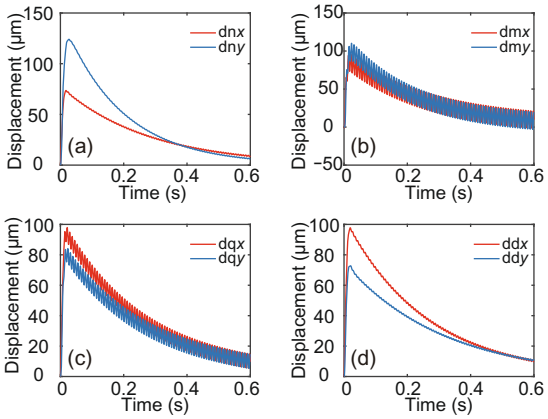

Fig. 11 Rotor displacements at $\Omega = 7600$ r/min of an emulated flywheel with $J_p = 0.021$ kg·m^2 and Δi=0.3 A, under characteristic model based ACAC laws: (a) NDE; (b) MID; (c) QTR; (d) DE

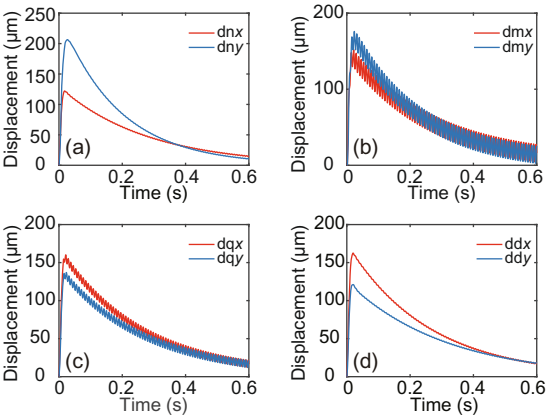

Fig. 12 Rotor displacements at $\Omega = 7600$ r/min of an emulated flywheel with $J_p = 0.021$ kg·m^2 and Δi=0.5 A, under characteristic model based ACAC laws: (a) NDE; (b) MID; (c) QTR; (d) DE

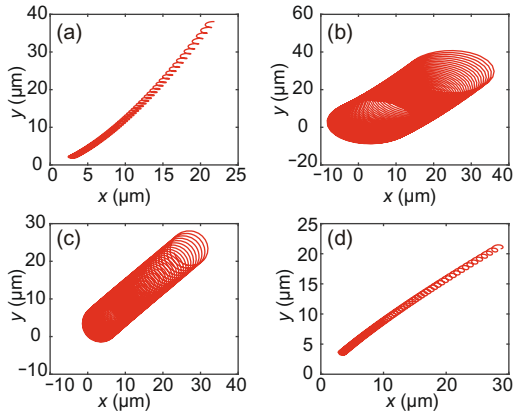

Fig. 13 Rotor orbits at $\Omega = 7600$ r/min of an emulated flywheel with $J_p = 0.021$ kg·m^2 and Δi=0.1 A, under characteristic model based ACAC laws: (a) dn$x$-dn$y$; (b) dm$x$-dm$y$; (c) dq$x$-dq$y$; (d) dd$x$-dd$y$

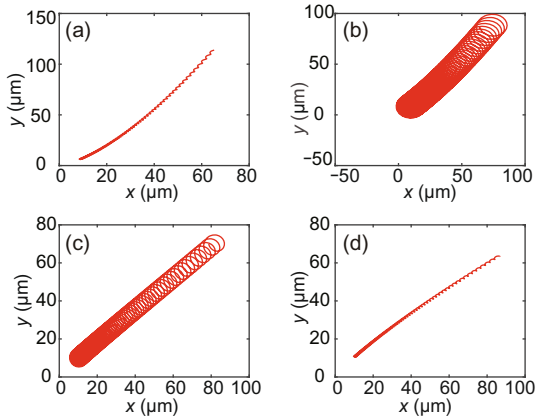

Fig. 14 Rotor orbits at $\Omega = 7600$ r/min of an emulated flywheel with $J_p = 0.021$ kg·m^2 and Δi=0.3 A, under characteristic model based ACAC laws: (a) dn$x$-dn$y$; (b) dm$x$-dm$y$; (c) dq$x$-dq$y$; (d) dd$x$-dd$y$

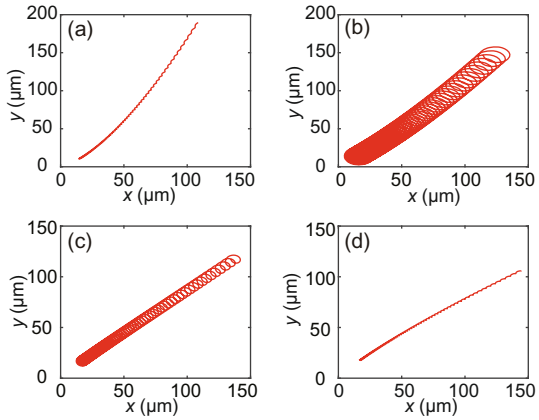

Fig. 15 Rotor orbits at $\Omega = 7600$ r/min of an emulated flywheel with $J_p = 0.021$ kg·m^2 and Δi=0.5 A, under characteristic model based ACAC laws: (a) dn$x$-dn$y$; (b) dm$x$-dm$y$; (c) dq$x$-dq$y$; (d) dd$x$-dd$y$

Table 1 Peak values of the rotor displacements at $\Omega = 7600$ r/min of an emulated flywheel with $J_p = 0.021$ kg·m^2 and Δi=0.1, 0.3, and 0.5 A, under characteristic model based ACAC laws

Location	Peak value (μm)		
	$\Delta i = 0.1$ A	$\Delta i = 0.3$ A	$\Delta i = 0.5$ A
dn$x$	25	74	122
dn$y$	42	124	207
dm$x$	41	95	152
dm$y$	45	110	176
dq$x$	37	98	159
dq$y$	31	84	137
dd$x$	33	98	162
dd$y$	25	73	121

4.2 Sinusoidal disturbances

We consider the periodic disturbances. In the simulations, we introduced sinusoidal disturbances

$\Delta i = 0.5\sin(\omega t)$ at the inputs of all four AMBs. The frequency of these disturbances is synchronous with the rotational speed of Ω =7600 r/min. Figs. 16 and 17 show the rotor displacements and rotor orbits at the locations of the four AMBs with polar moment of inertia $J_\mathrm{p} = 0.021\,\mathrm{kg{\cdot}m^2}$ and at the rotational speed of Ω =7600 r/min, respectively. Also, the same characteristic model based ACAC laws in Fig. 9 were applied. Table 2 summarizes the maximum amplitudes of the rotor displacements at the locations of the four AMBs at the x and y axes. It is observed that the system maintains a stable operation with persistent periodic disturbances at the four AMBs.

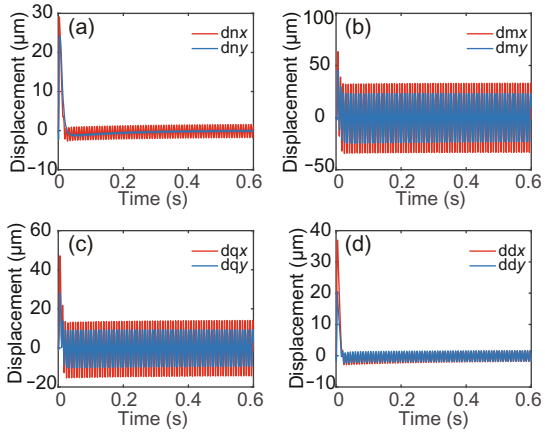

Fig. 16 Rotor displacements at $\Omega = 7600$ r/min of an emulated flywheel with $J_\mathrm{p} = 0.021\ \mathrm{kg{\cdot}m^2}$ and $\Delta i = 0.5\sin(\omega t)$, under characteristic model based ACAC laws: (a) NDE; (b) MID; (c) QTR; (d) DE

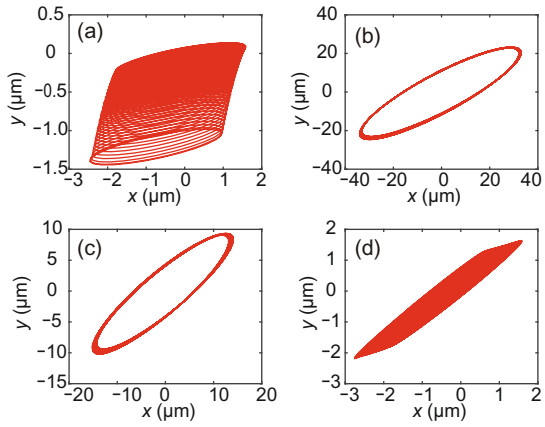

Fig. 17 Rotor orbits at $\Omega = 7600$ r/min of an emulated flywheel with $J_\mathrm{p} = 0.021\ \mathrm{kg{\cdot}m^2}$ and $\Delta i = 0.5\sin(\omega t)$, under characteristic model based ACAC laws: (a) dn$x$-dn$y$; (b) dm$x$-dm$y$; (c) dq$x$-dq$y$; (d) dd$x$-dd$y$

Table 2 Peak values of the rotor displacements at $\Omega = 7600$ r/min of an emulated flywheel with $J_\mathrm{p} = 0.021\ \mathrm{kg{\cdot}m^2}$ and $\Delta i = 0.5\sin(\omega t)$, under characteristic model based ACAC laws

Location	Peak value (μm)
dn$x$	29.1
dn$y$	24.2
dm$x$	63.2
dm$y$	45.3
dq$x$	47.2
dq$y$	28.1
dd$x$	37.0
dd$y$	20.5

5 Robustness with respect to time delays

Because of the limited speed of signal transmission and information processing, time delay is inevitable especially when the electronic components of the flywheel AMB control system are placed at a distance from the flywheel; e.g., in some applications in tidal power generation and wind power generation, the flywheel AMB systems serve as energy storage devices. In addition to the presence of external disturbances, as examined in Section 4.1, we introduce control input delays and sensor output delays to the flywheel AMB systems.

5.1 Control input delays

We consider the input delays in this subsection. The rotor displacements and rotor orbits of the flywheel AMB test rig under the characteristic model based ACAC laws, with a control input delay of one sampling period of the digital controller $\tau = T_\mathrm{s}$ and constant disturbance of Δi=0.1 A, are shown in Figs. 18 and 19, respectively. Table 3 presents the peak rotor displacements at the locations of the four AMBs. It is observed that the characteristic model based ACAC laws can resist the simultaneous effects of time delay $\tau = T_\mathrm{s}$ in the control input and constant disturbance Δi=0.1 A.

5.2 Sensor output delays

We consider the effect of sensor output delays. Rotor displacements and rotor orbits with a sensor output delay of one sampling period of the digital controller and the constant disturbance of Δi=0.1 A are shown in Figs. 20 and 21, respectively. Table 4

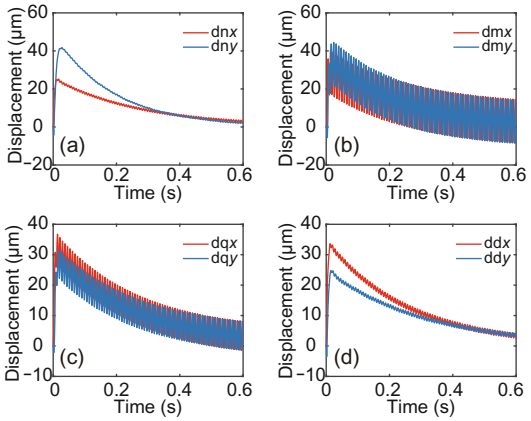

Fig. 18 Rotor displacements at $\Omega = 7600$ r/min of an emulated flywheel with $J_p = 0.021$ kg·m^2, Δi=0.1 A, and control input delay $\tau = T_s$, under characteristic model based ACAC laws: (a) NDE; (b) MID; (c) QTR; (d) DE

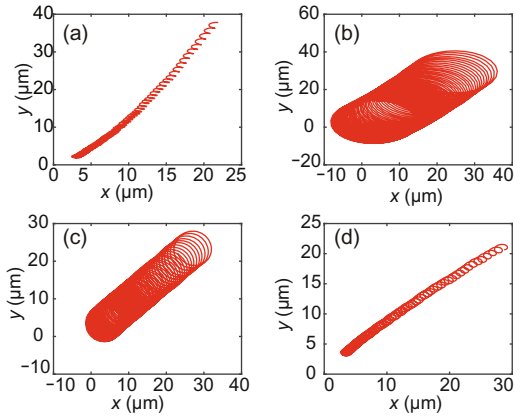

Fig. 19 Rotor orbits at $\Omega = 7600$ r/min of an emulated flywheel with $J_p = 0.021$ kg·m^2, Δi=0.1 A, and control input delay $\tau = T_s$, under characteristic model based ACAC laws: (a) dn$x$-dn$y$; (b) dm$x$-dm$y$; (c) dq$x$-dq$y$; (d) dd$x$-dd$y$

Table 3 Peak values of the rotor displacements at $\Omega = 7600$ r/min of an emulated flywheel with $J_p = 0.021$ kg·m^2, Δi=0.1 A, and control input delay $\tau = T_s$, under characteristic model based ACAC laws

Location	Peak value (μm)
dn$x$	25.2
dn$y$	41.7
dm$x$	41.1
dm$y$	44.5
dq$x$	36.8
dq$y$	31.6
dd$x$	33.7
dd$y$	24.8

shows the peak rotor displacements at the locations of the four AMBs. It is observed that the flywheel AMB systems remain stable with simultaneous sensor output delays and constant disturbances.

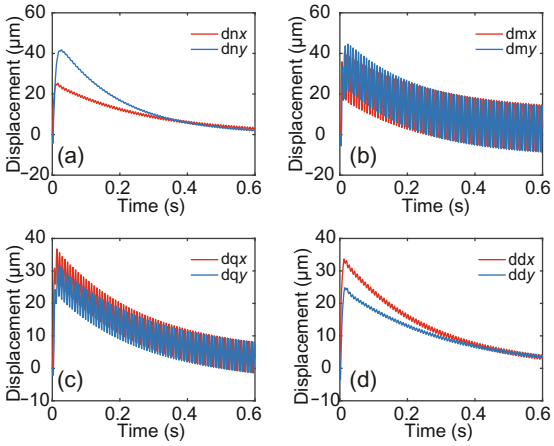

Fig. 20 Rotor displacements at $\Omega = 7600$ r/min of an emulated flywheel with $J_p = 0.021$ kg·m^2, Δi=0.1 A, and sensor output delay $\tau = T_s$, under characteristic model based ACAC laws: (a) NDE; (b) MID; (c) QTR; (d) DE

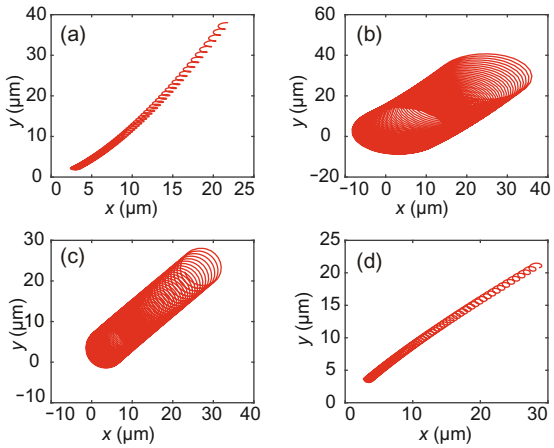

Fig. 21 Rotor orbits at $\Omega = 7600$ r/min of an emulated flywheel with $J_p = 0.021$ kg·m^2, Δi=0.1 A, and sensor output delay $\tau = T_s$, under characteristic model based ACAC laws: (a) dn$x$-dn$y$; (b) dm$x$-dm$y$; (c) dq$x$-dq$y$; (d) dd$x$-dd$y$

Table 4 Peak values of the rotor displacements at $\Omega = 7600$ r/min of an emulated flywheel with $J_p = 0.021$ kg·m^2, Δi=0.1 A, and sensor output delay $\tau = T_s$, under characteristic model based ACAC laws

Location	Peak value (μm)
dn$x$	25.3
dn$y$	41.8
dm$x$	41.1
dm$y$	44.3
dq$x$	36.8
dq$y$	31.6
dd$x$	33.7
dd$y$	24.8

5.3 Delays at control inputs and sensor outputs

We now consider the simulation with both control input delay and sensor output delay. Figs. 22 and 23 show the flywheel rotor displacements and rotor orbits with both control input delay and sensor output delay equal to T_s and a constant disturbance Δi=0.1 A. The peak values of the rotor displacements at the locations of the four AMBs are shown in Table 5. These results clearly show that the characteristic model based ACAC laws can resist the simultaneous influence of control input delay, sensor output delay, and constant disturbances.

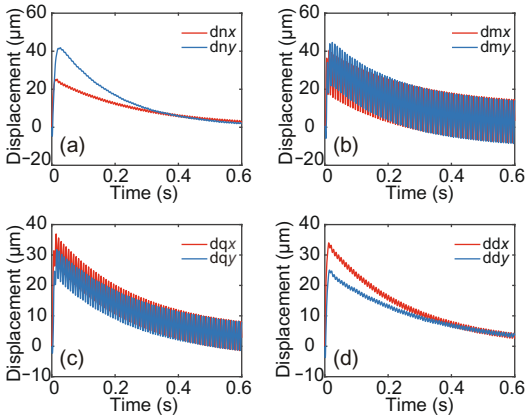

Fig. 22 Rotor displacements at Ω = 7600 r/min of an emulated flywheel with J_p = 0.021 kg·m^2, Δi=0.1 A, control input delay $\tau = T_s$, and sensor output delay $\tau = T_s$, under characteristic model based ACAC laws: (a) NDE; (b) MID; (c) QTR; (d) DE

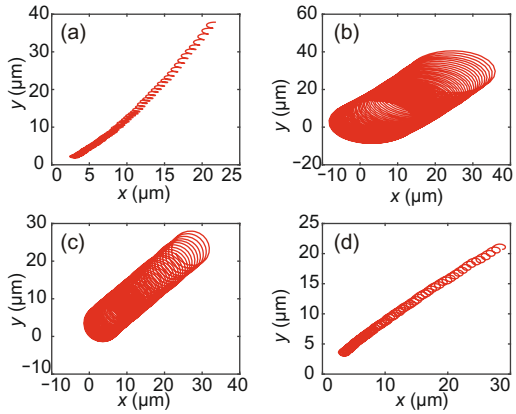

Fig. 23 Rotor orbits at Ω = 7600 r/min of an emulated flywheel with J_p = 0.021 kg·m^2, Δi=0.1 A, control input delay $\tau = T_s$, and sensor output delay $\tau = T_s$, under characteristic model based ACAC laws: (a) dn$x$-dn$y$; (b) dm$x$-dm$y$; (c) dq$x$-dq$y$; (d) dd$x$-dd$y$

Table 5 Peak values of the rotor displacements at Ω = 7600 r/min of an emulated flywheel with J_p = 0.021 kg·m^2, Δi=0.1 A, control input delay $\tau = T_s$, and sensor output delay $\tau = T_s$, under characteristic model based ACAC laws

Location	Peak value (μm)
dn$x$	25.3
dn$y$	41.8
dm$x$	41.4
dm$y$	44.6
dq$x$	36.9
dq$y$	31.8
dd$x$	34.0
dd$y$	25.1

6 Conclusions

In this paper, we have investigated the robustness of the characteristic model based all-coefficient adaptive control (ACAC) on an AMB suspended energy storage flywheel test rig with respect to plant uncertainties, external disturbances, and time delay. The experimental platform for AMB suspended energy storage flywheel, developed from an existing flexible rotor-AMB test rig in the ROMAC Laboratory at the University of Virginia, has been reviewed. The rotor behaviors of the flywheel emulation platform under the characteristic model based ACAC have been briefly presented. The performances of the closed-loop flywheel AMB systems with plant uncertainties, external disturbances, and time delay have been tested in the simulations. Extensive and systematic simulations demonstrated that the characteristic model based ACAC possesses considerable robustness with respect to plant uncertainties, external disturbances, and time delay.

References

Brown GV, Kascak AF, Jansen RH, et al., 2005. Stabililizing gyroscopic modes in magnetic-bearing-supported flywheels by using cross-axis proportional gains. Proc AIAA Guidance, Navigation, and Control Conf and Exhibit, p.5955. https://doi.org/10.2514/6.2005-5955

Dever TP, Brown GV, Duffy KP, et al., 2004. Modeling and development of magnetic bearing controller for high speed flywheel system. 2nd Int Energy Conversion Engineering Conf, p.5626. https://doi.org/10.2514/6.2004-5626

Di L, Lin ZL, 2014. Control of a flexible rotor active magnetic bearing test rig: a characteristic model based all-coefficient adaptive control approach. *Contr Theor Technol*, 12(1):1-12. https://doi.org/10.1007/s11768-014-0184-0

Farhadi M, Mohammed O, 2016. Energy storage technologies for high-power applications. *IEEE Trans Ind Appl*, 52(3):1953-1961. https://doi.org/10.1109/TIA.2015.2511096

Hebner R, Beno J, Walls A, 2002. Flywheel batteries come around again. *IEEE Spectr*, 39(4):46-51. https://doi.org/10.1109/6.993788

Koohi-Kamali S, Tyagi VV, Rahim NA, et al., 2013. Emergence of energy storage technologies as the solution for reliable operation of smart power systems: a review. *Renew Sust Energ Rev*, 25:135-165. https://doi.org/10.1016/j.rser.2013.03.056

Li GX, Lin ZL, Allaire PE, et al., 2006. Modeling of a high speed rotor test rig with active magnetic bearings. *J Vibr Acoust*, 128(3):269-281. https://doi.org/10.1115/1.2172254

Lyu XJ, Di L, Yoon SY, et al., 2016. A platform for analysis and control design: emulation of energy storage flywheels on a rotor-AMB test rig. *Mechatronics*, 33:146-160. https://doi.org/10.1016/j.mechatronics.2015.12.007

Lyu XJ, Di L, Lin ZL, et al., 2018a. Characteristic model based all-coefficient adaptive control of an AMB suspended energy storage flywheel test rig. *Sci China Inform Sci*, 61(11):112204. https://doi.org/10.1007/s11432-017-9327-0

Lyu XJ, Di L, Lin ZL, et al., 2018b. Performance of AMB suspended energy sorage flywheel controllers in the presence of time delays. 16$^{\text{th}}$ Int Symp on Magentic Bearings.

Mousavi G SM, Faraji F, Majazi A, et al., 2017. A comprehensive review of flywheel energy storage system technology. *Renew Sust Energ Rev*, 67:477-490. https://doi.org/10.1016/j.rser.2016.09.060

Mushi SE, Lin Z, Allaire PE, 2012. Design, construction, and modeling of a flexible rotor active magnetic bearing test rig. *IEEE/ASME Trans Mechatron*, 17(6):1170-1182. https://doi.org/10.1109/TMECH.2011.2160456

Peng C, Fan YH, Huang ZY, et al., 2017. Frequency-varying synchronous micro-vibration suppression for a MSFW with application of small-gain theorem. *Mech Syst Sign Process*, 82:432-447. https://doi.org/10.1016/j.ymssp.2016.05.033

Reid CM, Miller TB, Hoberecht MA, et al., 2013. History of electrochemical and energy storage technology development at NASA Glenn research center. *J Aerosp Eng*, 26(2):361-371. https://doi.org/10.1061/(ASCE)AS.1943-5525.0000323

Schweitzer G, Maslen EH, 2009. Magnetic Bearings: Theory, Design, and Application to Rotating Machinery. Springer Berlin, Germany.

Sivrioglu S, Nonami K, Saigo M, 2004. Low power consumption nonlinear control with H_∞ compensator for a zero-bias flywheel AMB system. *Mod Anal*, 10(8):1151-1166. https://doi.org/10.1177/1077546304043544

Wu HX, Hu J, Xie YC, 2007. Characteristic model-based all-coefficient adaptive control method and its applications. *IEEE Trans Syst Man Cybern Part C (Appl Rev)*, 37(2):213-221. https://doi.org/10.1109/TSMCC.2006.887004

Wu HX, Hu J, Xie YC, 2009. Characteristic Model-Based and Intelligent Adaptive Control. Science and Technology Press of China, Beijing, China (in Chinese).

Zhao HR, Wu QW, Hu SJ, et al., 2015. Review of energy storage system for wind power integration support. *Appl Energy*, 137:545-553. https://doi.org/10.1016/j.apenergy.2014.04.103